

# The Sun's Preferred Longitudes and the Coupling of Magnetic Dynamo Modes.

Alberto Bigazzi and Alexander Ruzmaikin

*Jet Propulsion Laboratory, California Institute of Technology, CA USA*

## ABSTRACT

Observations show that solar activity is distributed non-axisymmetrically, concentrating at “preferred longitudes”. This indicates the important role of non-axisymmetric magnetic fields in the origin of solar activity. We investigate the generation of the non-axisymmetric fields and their coupling with axisymmetric solar magnetic field. Our kinematic generation (dynamo) model operating in a sphere includes solar differential rotation, which approximates the differential rotation obtained by inversion of helioseismic data, modelled distributions of the turbulent resistivity, non-axisymmetric mean helicity, and meridional circulation in the convection zone. We find that (1) the non-axisymmetric modes are localised near the base of the convection zone, where the formation of active regions starts, and at latitudes around  $30^\circ$ ; (2) the coupling of non-axisymmetric and axisymmetric modes causes the non-axisymmetric mode to follow the solar cycle; the phase relations between the modes are found. (3) The rate of rotation of the first non-axisymmetric mode is close to that determined in the interplanetary space.

*Subject headings:* Sun: magnetic fields — MHD

## 1. Introduction

Solar magnetic activity tends to cluster at “preferred longitudes” (Vitinskij 1969 ; Bogart 1982; Bai 1987; Antonucci et al. 1990; Benevolenskaya et al. 1999; de Toma et al. 2000). Spacecraft data collected over three solar cycles indicate a persistent dependence of the solar wind speed and the radial component of the interplanetary magnetic field on solar longitude. Patterns are found to be rotating with a fixed period (Neugebauer et al. 2000). This indicates the involvement of non-axisymmetric (i.e. longitude dependent) large-scale magnetic fields in the formation and evolution of solar activity as seen in solar magnetograms (Ruzmaikin et al. 2001; Henney & Harvey 2003).

The direct expansion of observed solar magnetograms into spherical harmonics shows the presence of axisymmetric (longitude-independent) and non-axisymmetric modes (Altschuler et al. 1974; de Toma et al. 2000). The axisymmetric mode dominates at solar minimum and the first non-axisymmetric mode is prevalent at solar max-

imum (Ruzmaikin et al. 2001). Earlier studies (Stix 1974; Krause & Rädler 1980; Ivanova & Ruzmaikin 1985) have shown that non-axisymmetric modes could be generated by the mean-field dynamo under certain constraints imposed on the distributions of the differential rotation and the mean kinetic helicity ( $\alpha$ -effect). These earlier studies did not include the correct distribution, in radius and latitude, of the solar differential rotation curve, unknown at the time. A more recent model of Moss (1999), which includes the updated rotation curve, also displays the generation of a non-axisymmetric component of the field.

The non-axisymmetric magnetic fields are generated by axisymmetric sources but, in kinematic mean-field dynamos, evolve independently of the axisymmetric field. In particular, the non-axisymmetric modes do not have the same period as the axisymmetric mode. However, the observation that in the Sun the non-axisymmetric fields do have the same solar cycle as the axisymmetric fields, suggests a coupling between the modes that locks the oscillation periods of the two together.

Here we prove that this is in fact possible and it can be achieved by relaxing the assumption of axisymmetry for the  $\alpha$ -effect.

The coupling of different modes by non-axisymmetric motions was first studied for the Earth's magnetic fields by Bullard & Gellman (1954). Non-axisymmetry is a key ingredient in models of tachocline solar flux tube dynamics that studied the instabilities leading to rise of the flux tubes (Choudhuri 1989; Fan et al. 1993; Ferriz-Mas & Shüssler 1994; Caligari et al. 1995; 1998). In these models the formation of magnetic loops emerging at the solar surface as active regions is considered to be a consequence of these non-axisymmetric (kink-type) instabilities. Although the dynamo itself is not treated in these studies, longitudinal instabilities are connected to the emergence of active regions, see also Ruzmaikin (2001). A calculation of the  $\alpha$ -effect from these instabilities, have been performed by (Ferriz-Mas et al. 1994). Such an  $\alpha$ -effect, however, has not yet been included in mean-field dynamo models. Kinetic helicity in hydrodynamic simulation of shallow water instabilities used in models of the tachocline, also reveal a non-axisymmetric,  $m = 1$ , pattern for the  $\alpha$ -effect (Dikpati & Gilman 2001). That is not included, however, in the dynamo model that the same authors have analysed. A non-axisymmetric  $\alpha$ -effect has been considered in mean-field dynamo models of the galactic dynamo (Moss et al. 1991).

Here for the first time we study the solar mean-field dynamo with a non-axisymmetric  $\alpha$ . We discuss the distribution in radius latitude and azimuth of the first non-axisymmetric mode and relate it to preferred longitudes and clustering of magnetic activity. It is important to note that, contrary to the axisymmetric fields, the non axisymmetric modes are rotating structures in the frame of reference of the body. The rate of rotation of these modes is determined by the solution of the dynamo equations. We determine the rate for the  $m = 1$  mode by looking at the evolution of the surface patterns of its radial magnetic field. Because the surface poloidal field expands into the solar wind, we relate this rate to the signatures of preferred longitudes found in the solar wind.

Our kinematic model includes an approximation to the helioseismically observed distribution of the differential rotation and modelled distributions of other sources of the mean field generation.

## 2. The Non-Axisymmetric Dynamo Model

When the motions are given, the generation of the mean magnetic field is described by the equations

$$\partial_t \mathbf{B} = \nabla \times (\mathbf{u} \times \mathbf{B} + \alpha \mathbf{B} - \eta \mathbf{B}), \quad (1)$$

$$\nabla \cdot \mathbf{B} = 0 \quad (2)$$

(Moffat 1978; Parker 1979; Krause & Rädler 1980), where  $\mathbf{B}$  is the mean magnetic field (the first statistical moment of the total field),  $\mathbf{u}$  is the mean velocity,  $\alpha$  is the mean-helicity, and  $\eta$  is the electrical resistivity, which includes the turbulent resistivity.

Solar rotation is approximated by a simple analytical fit (Charbonneau et al. 1999; Moss 1999) to the distribution reconstructed by helioseismic methods (Kosovichev 1996; Howe et al. 2000), see Fig. 1. Details are given in the Appendix. The rate of the equatorial rotation is taken as  $\Omega_{eq}/2\pi = 460.7 \text{ nHz} = 4.607 \times 10^{-9} \text{ s}^{-1}$ . This distribution matches the core rotation  $\Omega_c$  smoothly in a layer of thickness  $0.04R_\odot$  at  $0.69R_\odot$ . The core rotation is about equal to the surface rotation  $\Omega_s$  at  $30^\circ$  latitude. The surface shear layer is not included in this model. However, the deep shear layer at  $0.7R_\odot$ , i.e. the tachocline, is well approximated.

The distribution of  $\alpha$  cannot yet be determined from observations. We therefore consider three typical cases, see Appendix. The radial profiles are shown in Fig. 2. In the first case, M1, the distribution of  $\alpha$  is independent of radius in the convection zone and rapidly decreases below the convection zone. In the second case, M2,  $\alpha$  is concentrated near the solar surface and does not overlap with the shear layer. In the third case, M3,  $\alpha$  is localised above the tachocline (Charbonneau & MacGregor 1997; Mason et al. 2002) overlapping with the radial shear. The latitudinal dependence of  $\alpha$  in all three cases is assumed to be  $\cos\theta$ . This simple angular dependence is partially justified by the fact that the pseudo-scalar  $\alpha$  can be formed from the scalar product of the density gradient and rotation:  $\alpha \sim \nabla\rho \cdot \boldsymbol{\Omega} \sim \cos\theta$ . More elaborate angular dependences are produced by different models of  $\alpha$ , see for example Rüdiger & Brandenburg (1995), Dikpati & Gilman (2001), and can easily be incorporated into our model.

The resistivity  $\eta$  is taken constant throughout the convection zone with a sharp decrease in the transition layer to the highly conductive radiative interior. We consider the case when the transition layer is coincident with the rotational shear layer. For computational needs, we assume that the resistivity near the base of the convection zone is 50 to 200 times less than the turbulent resistivity in the bulk of the convection zone. (A realistic number would be of the order of  $10^6$ ). We use  $R_\odot^2/\eta$  as the time unit. We assign the value of the resistivity  $\eta$  by considering the marginal solution of model M1. We match the equatorial rotation rate in Fig. 1 to the observed one, obtaining  $\eta_0 = 2.74 \times 10^{11} \text{cm}^2 \text{s}^{-1}$ . Estimates made using classical mixing length theory, give a value for the resistivity of order  $10^{12} \text{cm}^2 \text{s}^{-1}$ .

The ratio  $T_c/T_{rot}$  of the cycle period to the rotation rate of the body is non-dimensional and does not therefore depend on the choice of  $\eta$ . For the Sun, the ratio of the cycle and the equatorial rotation rate, is approximately 150. Higher values of this number imply a cycle period of the solutions longer than the solar one. Shorter values, a shorter cycle period. We characterise the cycle periods of our solution in terms of this non-dimensional ratio.

In the case of non-axisymmetric dynamo an analogous ratio of the rate of rotation of the non-axisymmetric mode to the body rotation rate could also be used to characterise the solutions. Such a number clearly does not exist in the case of the axisymmetric dynamo where no rotating structures exist.

## 2.1. Mathematical Formulation and Numerical Procedure

We have developed a new code that solves the kinematic dynamo equations (1,2) in a spherical domain. We define a regular grid in the meridional circular sector  $r \in [r_{in}, R_\odot], \theta \in [0, \pi]$ , where  $\theta$  is the co-latitude. In the azimuthal direction  $\phi$  we expand all functions in m-modes,  $e^{im\phi}$ . Solving the equations in the real space has advantages over using the spectral Legendre Transform. The m-modal transform can be numerically performed in a very efficient way by means of the Fast Fourier Transform algorithm. No such algorithm exists for the Legendre Transform, needed for the latitudinal direction  $\theta$ . This makes spherical spectral codes

numerically expensive to run. It is also easier to parallelise a code in a regular domain.

We represent the divergence-free magnetic field by two scalar functions  $T$  and  $S$ , called the toroidal and poloidal potentials

$$\mathbf{B} = \underbrace{-\mathbf{r} \times \nabla T}_{\text{Toroidal}} + \underbrace{\nabla \times (-\mathbf{r} \times \nabla S)}_{\text{Poloidal}}. \quad (3)$$

(Moffat 1978; Krause & Rädler 1980). This representation ensures that the field is divergence free. The curl of a poloidal field is a toroidal field and vice versa.

The choice of  $T$  and  $S$  is made unique by means of the gauge condition

$$\int_\Sigma T \sin \theta \, d\theta \, d\phi = 0, \quad \int_\Sigma S \sin \theta \, d\theta \, d\phi = 0. \quad (4)$$

When the field vanishes,  $\mathbf{B} = 0$ , then its toroidal and poloidal components  $\mathbf{B}_p$  and  $\mathbf{B}_t$  vanish as well. The vector equation (1) therefore reduces to two coupled equations for the toroidal and poloidal potentials.

When  $\alpha = \alpha(r, \theta)$  and  $\eta = \eta(r)$ , the governing Eqs (1), in spherical coordinates  $r, \theta, \phi$ , reduce to

$$\begin{aligned} \partial_t T &= R_\Omega V_\Omega + R_\alpha V_\alpha + R_M V_M \\ &+ \eta \nabla^2 T + \partial_r \eta \cdot \frac{1}{r} \partial_r (rT), \\ \partial_t S &= R_\Omega U_\Omega + R_\alpha U_\alpha + R_M U_M \\ &+ \eta \nabla^2 S \end{aligned} \quad (5)$$

with the gauge conditions (4). The non-dimensional numbers  $R_\Omega, R_\alpha, R_M$  are defined as:

$$R_\Omega = \frac{\Omega_0 R_\odot^2}{\eta_0}, \quad R_\alpha = \frac{\alpha_0 R_\odot}{\eta_0}, \quad R_M = \frac{u_M R_\odot}{\eta_0}. \quad (6)$$

Subscripted quantities indicate typical amplitudes. The functions  $U_\Omega, V_\Omega, U_\alpha, V_\alpha, U_M, V_M$ , are related to the toroidal and poloidal parts of the sources:

$$((\boldsymbol{\Omega} \times \mathbf{r}) \times \mathbf{B})_T = -\mathbf{r} \times \nabla U_\Omega, \quad (7)$$

$$\nabla \times ((\boldsymbol{\Omega} \times \mathbf{r}) \times \mathbf{B})_P = -\mathbf{r} \times \nabla V_\Omega, \quad (8)$$

$$(\mathbf{u}_M \times \mathbf{B})_T = -\mathbf{r} \times \nabla U_M, \quad (9)$$

$$\nabla \times (\mathbf{u}_M \times \mathbf{B})_P = -\mathbf{r} \times \nabla V_M, \quad (10)$$

$$(\alpha \mathbf{B})_T = -\mathbf{r} \times \nabla U_\alpha, \quad (11)$$

$$\nabla \times (\alpha \mathbf{B})_P = -\mathbf{r} \times \nabla V_\alpha. \quad (12)$$

We have split the velocity field  $\mathbf{u}$  into its rotational (toroidal) and meridional components

$$\mathbf{u}(r, \theta) = \boldsymbol{\Omega}(r, \theta) \times \mathbf{r} + \mathbf{u}_M(r, \theta). \quad (13)$$

The functions  $U_\epsilon, V_\epsilon, U_\alpha, V_\alpha, U_M, V_M$  can be calculated from the above relations:

$$-L^2 V_\Omega = \mathbf{r} \cdot \nabla \times \nabla \times ((\boldsymbol{\Omega} \times \mathbf{r}) \times \mathbf{B}), \quad (14)$$

$$-L^2 U_\Omega = \mathbf{r} \cdot \nabla \times ((\boldsymbol{\Omega} \times \mathbf{r}) \times \mathbf{B}), \quad (15)$$

$$-L^2 V_M = \mathbf{r} \cdot \nabla \times \nabla \times (\mathbf{u}_M \times \mathbf{B}), \quad (16)$$

$$-L^2 U_M = \mathbf{r} \cdot \nabla \times (\mathbf{u}_M \times \mathbf{B}), \quad (17)$$

$$-L^2 V_\alpha = \mathbf{r} \cdot \nabla \times \nabla \times (\alpha(r, \theta) \mathbf{B}), \quad (18)$$

$$-L^2 U_\alpha = \mathbf{r} \cdot \nabla \times (\alpha(r, \theta) \mathbf{B}), \quad (19)$$

where

$$L^2 = \frac{1}{\sin \theta} \frac{\partial}{\partial \theta} \left( \sin \theta \frac{\partial}{\partial \theta} \right) + \frac{1}{\sin^2 \theta} \frac{\partial^2}{\partial \phi^2} \quad (20)$$

is the angular part of the Laplacian operator

$$\nabla^2 = \frac{1}{r^2} \frac{\partial}{\partial r} r^2 \frac{\partial}{\partial r} + \frac{1}{r^2} L^2. \quad (21)$$

The inversions in Eqs.(14-19) can be efficiently carried out numerically.

## 2.2. The m-Modal Expansion

We expand all functions  $T, S, V, U$  in Eq. (5) into the m-modes

$$T(r, \theta, \phi) = \sum_{m=0}^N T^m(r, \theta) e^{im\phi} + cc, \dots \quad (22)$$

where  $T^m(r, \theta)$  are complex functions and  $N$  is the maximum order of the expansion. When the sources  $(\mathbf{u}, \alpha, \eta)$  are axisymmetric, i.e. do not depend on the azimuth  $\phi$ , Eqs. (5) decouple into a set of  $2(N+1)$  equations.

$$\begin{aligned} \partial_t T^m &= R_\Omega V_\Omega^m + R_\alpha V_\alpha^m + R_M V_M^m \\ &+ \eta \nabla_m^2 T_\Omega^m + \partial_r \eta(r) \frac{1}{r} \partial_r (r T^m), \\ \partial_t S^m &= R_\Omega U_\Omega^m + R_\alpha U_\alpha^m + R_M U_M^m \\ &+ \eta \nabla_m^2 S^m. \end{aligned} \quad (23)$$

where  $\nabla_m^2$  is the Laplacian operator (21), in which  $\partial^2/\partial^2\phi$  is replaced by  $-m^2$ . Each of the m-modes can therefore be found from an independent set of equations. The functions  $U^m, V^m, U_\alpha^m, V_\alpha^m$ ,

$U_M^m$ , and  $V_M^m$ , are solutions of the m-transformed equations (14-19), such as:

$$\begin{aligned} &[-L^2]^m U_\alpha^m(r, \theta) \cdot e^{im\phi} = \\ &= [\mathbf{r} \cdot \nabla \times]^m \alpha \mathbf{B}^m(r, \theta) \cdot e^{im\phi}, \end{aligned} \quad (24)$$

$$\begin{aligned} &[-L^2]^m V_\alpha^m(r, \theta) \cdot e^{im\phi} = \\ &= [\mathbf{r} \cdot \nabla \times \nabla \times]^m \alpha \mathbf{B}^m(r, \theta) \cdot e^{im\phi}, \end{aligned} \quad (25)$$

for the potentials  $U_\alpha^m, V_\alpha^m$ . Analogous expressions can be found for the other potentials in Eqs. (14-19). The operators  $[\mathbf{r} \cdot \nabla \times]^m, [\mathbf{r} \cdot \nabla \times \nabla \times]^m$  and  $[-L^2]^m$  are the m-transformed operators, where the derivatives with respect to  $\phi$  become multiplications by the complex factor  $im$ .

We solve the set of equations (23) numerically. At each time step, we solve Eqs. (24,25) and the corresponding equations for the  $\mathbf{u} \times \mathbf{B}$  term for the auxiliary potentials  $v_\Omega^m, U_\Omega^m, v_M^m, U_M^m, U_\alpha^m, V_\alpha^m$ . Equations (23) are then advanced in time with a third-order Runge Kutta method. Spatial derivatives are second-order accurate in a regular  $[r, \theta]$  mesh. The models below have the resolution of 80x160 mesh points.

## 2.3. Coupling of the Modes

When the assumption of axisymmetry for  $\alpha$  is relaxed, the set of dynamo equations (23), for each  $m$ , are no longer independent. But it is still possible to use Eqs.(24,25), where the product  $\alpha(r, \theta) \mathbf{B}^m$  is replaced by the convolution

$$(\alpha \mathbf{B})^m = \sum_{j=-\infty}^{\infty} \alpha^j(r, \theta) \mathbf{B}^{m-j}(r, \theta). \quad (26)$$

The coefficients with negative indices are equivalent to the complex conjugate of the coefficient with the positive indices.

We investigate in detail the simplest situation of coupling of  $m = 0$  and  $m = 1$  modes, retaining only the lowest  $m = 0$  and  $m = 1$  terms in the expansion (26). The contribution to the  $m = 1$  mode thus becomes:

$$(\alpha \mathbf{B})^1 = \alpha^0 \mathbf{B}^1 + \epsilon \alpha^1 \mathbf{B}^0. \quad (27)$$

The non-axisymmetric part of  $\alpha$  ( $\alpha^1$ ) thus introduces a linear coupling between the  $m = 1$  and the  $m = 0$  modes. The amplitude of the resulting

non-axisymmetric field depends on the value of  $\epsilon$ . In the results displayed below,  $\epsilon = 1$  is used in model M1 and  $\epsilon = 0.2$  in models M2 and M3. For an  $\alpha\Omega$  dynamo, when  $R_\omega \gg R_\alpha$ , Eq. (27) means that the poloidal  $m = 1$  component of the field is driven by the toroidal  $m = 0$  component. The toroidal  $m = 0$ ,  $m = 1$  modes are related respectively to the poloidal  $m = 0$ ,  $m = 1$  modes by the differential rotation.

## 2.4. Boundary conditions

The conditions on the rotation axis  $\theta = 0$  are different for different values of  $m$ . For even  $m$ , any function maps into itself when  $\phi \rightarrow \phi + \pi$  and therefore on the axis the derivative in the  $\theta$ -direction perpendicular to the axis must vanish. For odd  $m$  every function subjected to this mapping is multiplied by  $-1$  and therefore must vanish on the axis ( $\theta = 0$ ) to satisfy continuity. Hence,

$$\frac{\partial S}{\partial \theta} = \frac{\partial T}{\partial \theta} = 0, \quad m = 0, \quad (28)$$

$$S = T = 0, \quad m = 1. \quad (29)$$

We consider a spherical shell  $r_{in} < R_\odot < 1$  with internal radius  $r_{in} = 0.4R_\odot$ , where we define our potentials  $S, T$  to be zero. The physical boundary between the core and the convection zone is identified by the sharp change in electrical resistivity at  $0.69R_\odot$ . The computational domain extends further down, to  $0.4R_\odot$ . We allow enough time for the diffusion and differential rotation to expel the flux from the low-conductivity region.

On the outer boundary,  $r = R$ , we adopt the potential (vacuum) field conditions:

$$T = 0, \quad \frac{\partial S_\ell^m}{\partial r} + \frac{(\ell + 1)}{R} S_\ell^m = 0, \quad (30)$$

where  $S_\ell^m$  are the coefficients of the decomposition into spherical harmonics of degree  $\ell$  and order  $m$  of the scalar potential  $S$  at the surface. For the numerical scheme, which is second order in the  $r$ -direction, we only need to solve this equation at two  $r$ -layers which are next to the boundary.

## 2.5. Meridional Circulation

Meridional circulation has long been observed on the surface of the Sun with a variety of techniques from sunspot tracking (Tuominen 1941) to

Doppler and helioseismic measures (LaBonte & Howard 1982; Hathaway et al. 1996; Haber et al. 2002).

The patterns correspond to a single-cell large-scale flow proceeding from the equator to the pole with an amplitude at the surface of about 20 m/s. Recent measurements indicate, however, that the flow might in fact have a more complex nature, even reversing at times and showing a non-trivial vertical structure (Haber et al. 2002).

With current techniques, the upper 15% of the solar surface can be probed (Braun & Fan 1998). The return flow is not observed although some progress has been made in this direction (Giles et al. 1997). In particular, the depth into the convection zone to which it penetrates is not known. Hathaway et al. (2003) examine the drift of the centroid of the sunspot area toward the equator in each hemisphere from 1874 to 2002 and find that these observations are consistent with a meridional counterflow deep within the Sun as the primary driver of the migration toward the equator and the period associated with the sunspot cycle.

In the context of an axisymmetric dynamo, meridional circulation has been extensively studied (Roberts & Stix 1972; Wang et al. 1991; Choudhuri et al. 1995; Durney 1995; Dikpati & Gilman 2001; Nandy & Choudhuri 2002). For the magnetic fields to be effectively transported by such a small amplitude flow, the electrical resistivity has to be low, a condition that is fulfilled below the convection zone, where resistivity and turbulence dramatically decrease. Hence, one can expect that a deep flow, sinking below the convection zone, will be more effective in acting upon the field (Nandy & Choudhuri 2002). However, it has not been established that such a flow can realistically exist. We will discuss two models, see Fig. 3.

## 2.6. Initial Conditions

We select an initial field of antisymmetric (dipolar) symmetry with respect to the equator by choosing the following potentials for  $m = 0$  and  $m = 1$  modes:

$$\begin{aligned} S(t = 0) &= S_1^0, & S^1(t = 0) &= S_2^1, \\ T(t = 0) &= T_2^0, & T^1(t = 0) &= T_1^1. \end{aligned} \quad (31)$$

Here,  $S_l^m$  indicates a function proportional to the spherical harmonic of order  $l$  and degree  $m$ . No symmetry with respect to the equator is imposed

on the time-dependent solution, and the whole domain  $\theta \in [0, \pi]$  is therefore included.

The velocity field  $\mathbf{u}$  in the induction equation (1) is given. The induction equation is thus linear in the magnetic field  $\mathbf{B}$  and its solutions are exponentially growing or decaying in time. A stationary state is often achieved by introducing a quenching of the  $\alpha$ -effect when the field intensities exceed some level, for a discussion see for instance (Blackman & Field 2002). We do not prescribe here any quenching mechanism because it would introduce a further coupling between modes, making the interpretation of the results more complex. It would also add an element of arbitrariness, which is not necessary for our purposes. We will therefore be looking at solutions that are close to marginal excitation.

### 3. Results

We consider first the dynamo without meridional circulation ( $\mathbf{u}_M = 0$ ). In Table 1 the growth rate  $\gamma$ , the adimensional cycle period  $T$  and the ratio of the cycle period to the core rotation period  $T/T_{rot}$  as explained in Section 2, are given. The three models considered are labelled as M1, M2, M3. See also the Appendix for a more detailed description.

#### 3.1. Growth rates and cycle periods

The time evolution of the toroidal field potential for the M1 case is shown in Fig. 4. A steady exponential growth is reached after one diffusion time. We follow the run for approximately five diffusion times. However, already after  $t \sim 1$ , the solution appears to be stable. As seen in Fig. 4, the solution is oscillating. Each cycle lasts 179 rotations of the body being modelled. The ratio of the cycle period to the rotation rate, ( $T/T_{rot}$ ) is independent of the units adopted. This ratio discriminates between solutions that have a solar-like period and those which do not. For model M1, the ratio  $T/T_{rot}$  is 179 and is close to the solar case of 149.

Model M3, not shown, behaves similarly to model M1. It has a comparable oscillation period. The  $\alpha$ -effect in these two models have a broad radial distribution within the convection zone which overlaps with the shear layer, see Fig. 2.

In contrast, model's M2 behaviour is markedly

different than the previous two, especially regarding to the oscillation period  $T$ , which is ten times smaller than the cases M1 and M3.  $T/T_{rot}$  of 20.2 shows that M2 does not represent the solar case correctly. M2 is characterised by the  $\alpha$ -effect which has no overlap with the shear layer and this is probably the cause of its failure.

#### 3.2. Phase relations between the axisymmetric and non-axisymmetric modes

In Fig. 5 we show the time evolution of the radial and azimuthal components of the magnetic field during one cycle in model M3. The axisymmetric dipolar-type field at the pole reverses its sign when the (total) azimuthal field close to the tachocline is maximal. In other words, there is a phase shift of  $\pi/2$  between these two field components. We evaluate the toroidal fields at  $30^\circ$  of latitude, where the non-axisymmetric field is concentrated. For the plot of the  $m = 1$  component, which has the  $\cos\varphi$  dependence, we select the meridional plane defined by  $\varphi = 0$ , where the field is maximum. A similar relation is observed on the Sun: the axisymmetric dipole reverses close to the solar maximum. Analogous calculations for models M1 and M2 yield  $\pi/6$  and  $-3/4\pi$ , respectively, see Table 2. We may therefore conclude that the phase relation between the field components is dependent on the radial distribution of the  $\alpha$ -effect. This can help to select the models according to the phase relations between the field components, as originally indicated by Stix (1976).

Another phase relation that can be observed is the one between the surface axisymmetric and non-axisymmetric poloidal fields is shown in Figure 9 (Ruzmaikin et al. 2001). Note that, according to their definitions, the poloidal potentials have the same phase as the poloidal fields. For the purpose of determining the phase difference between the modes of the poloidal field, we can therefore use the potentials, see Figs. 6-8.

The time dependence of the  $m = 0$  and  $m = 1$  poloidal potentials is shown in Figs. 6-8. The phase relations can be read from the plot and are listed in Table 2.

### 3.3. Spatial distribution of the fields. Localisation of the non-axisymmetric modes

The poloidal field is found to be predominantly antisymmetric (odd) with respect to the equator (dipolar-type) in all three models. However, this symmetry is not pure and a symmetric component is present as well, see Fig. 10,11. We recall that we do not impose an equatorial symmetry conditions on the solution and solve the equations for the whole domain  $\theta \in [0, \pi]$ . The north-south symmetry is broken because we couple the axisymmetric mode, which is odd across the equator (like polar dipole), with the non-axisymmetric mode, which is even across the equator (like equatorial dipole). This north-south asymmetry does not disagree with observations. Fig. 12 shows the time evolution of the signed azimuthal magnetic field for the  $m = 1$  mode on the meridional plane  $\phi = 0$  during half of a cycle. In contrast to the axisymmetric mode, the non-axisymmetric field is highly concentrated in the lower part of the tachocline and, to lesser extent, near the surface. It is also localised around  $30^\circ$  latitude, see also Table (3).

In order to show the robustness of the spatial intensity distribution of the fields throughout a cycle we display the distribution of the absolute values of the the axisymmetric ( $m = 0$ ) and non-axisymmetric ( $m = 1$ ) toroidal fields inside the convection zone, integrated over a solar cycle (Figs. 13,14,15). In Table (3) we show the locations of the maxima of the toroidal  $m = 0$  and  $m = 1$  components,  $r_M^0$ ,  $\theta_M^0$ ,  $r_M^1$  and  $\theta_M^1$ .

The physical reason for these localisations can be understood. As it is well known from MHD theory (Moffat 1978; Krause & Rädler 1980), the differential rotation affects the axisymmetric and non-axisymmetric fields in different ways. Thus, an axisymmetric poloidal field in a differentially rotating region is converted into an axisymmetric toroidal field. But a non-axisymmetric field is rapidly (within a few rotations) excluded from the strongly differentially rotating high resistivity region. This happens because the rotation tends to twist the field lines perpendicular to the axis of rotation in such a way that any two adjacent lines would have an opposite direction. This leads to effective reconnection of these field lines, excluding the field from the differentially rotating

region even in the case of a very small electrical resistivity. Hence, differential rotation is a mechanism that tends to destroy any deviation from axial symmetry. In the solar convection zone, the field survives only in the regions where the differential rotation is weak (around  $30^\circ$ ) and where the resistivity is small, i.e. in the lower part of the tachocline.

The localisation of non-axisymmetric magnetic field suggests a simple explanation of why active regions emerging on the solar surface have a tendency to cluster on preferred longitudes. Active regions, such as sunspots, are the result of buoyancy of bipolar magnetic loops (flux ropes) through the solar surface, (Parker 1979). The flux ropes formed at the base of the convection zone emerge when their magnetic field exceeds the threshold for buoyancy. A non-axisymmetric enhancement of the underlying magnetic field at that location results in the clustering of active regions as shown in a heuristic model (Ruzmaikin 1998,2001). The  $m = 1$  mode of the toroidal magnetic field superimposed on the axisymmetric mode produces a localised field maximum (“hump”) near the maximum of  $\sin \phi$ . The humps, produced by non-axisymmetric fields, are unstable when their field strength reaches  $4 \times 10^4$  G (Caligari et al. 1995; 1998). Because the growth of the underlying non-axisymmetric mode is affected by the continuous stretching by differential rotation, the mode is after some time destroyed. The stretching time scale of several months is in agreement with the observed life-time of the clusters (Gaizauskas et al. 1983).

### 3.4. Rotation Rate and Preferred Longitudes

As we mentioned in the Introduction, a persistent, periodic magnetic pattern in the solar wind has been observed, with a fixed rotation rate (Neugebauer et al. 2000). A period consistent with this rate was also found from the surface fields (Ruzmaikin et al. 2001; Henney & Harvey 2003). If preferred longitudes are associated with the non-axisymmetric modes of the dynamo, then the observed pattern would originate in the poloidal non-axisymmetric component of the field.

The longitudinal distribution of the non-axisymmetric modes of the dynamo has the form of a wave

propagating along the azimuth  $\phi$  with a rate determined by the solution of the dynamo equations. We determine that rate,  $\Omega^1$ , by following the time evolution of the surface poloidal (radial)  $m = 1$  mode, Fig. 16. The results are given in Table 1 for the three models considered. We represent these rates as horizontal dashed lines, along with the radial distribution of the rotation rate, in Fig. 1.

The rotation rate of the non-axisymmetric  $m = 1$  mode is comparable to that of the surface rotation at  $30^\circ$  latitude for the M1 and M3 models. This is also the rotation rate of the core. For the M2 model, a slower rate is found. Recent Ulysses observations of the surface magnetic fields during Ulysses' fast scan around solar maximum, show a rotation rate of the non-axisymmetric dipole of the Sun close to the core rotation rate, see (Jones et al. 2003).

### 3.5. Meridional Circulation

The main goal of this paper is to study the excitation of the non-axisymmetric mode under otherwise simple conditions. For this purpose we did not include the meridional circulation in the models described above. Meridional circulation may play an important role in the overall dynamo, as indicated by other studies (Roberts & Stix 1972; Wang et al. 1991; Choudhuri et al. 1995; Durney 1995; Dikpati & Gilman 2001; Nandy & Choudhuri 2002). Here we report only on a preliminary analysis of two simple cases of meridional circulation for the M1 distribution of  $\alpha$ . The cases are (see Appendix): (1) shallow and (2) deep meridional circulation, see Fig. 3. In order to make the meridional transport more effective compared to diffusion in these calculations we decrease the ratio of the core resistivity to the resistivity in the convection zone to 1/200.

The resulting field distributions two cases are displayed in Figs. 17,18. Comparing these distributions with the case without meridional circulation, Fig. 13, we see that the field tends to be depleted in the upper part of the convection zone and intensified and stretched in the tachocline. This is especially true for the case with deep meridional circulation.

The field is pushed out of the convection zone into the tachocline, apparently under the action of the radial component of the circulation. The flow,

however, does not seem to be effective enough in the latitudinal direction to significantly change the toroidal field distribution, although there is a shift of its maximum below the  $30^\circ$  line (see Table 4).

A more significant change occurs in the cycle period of the solutions, which nearly doubles with an amplitude of the flow  $|\mathbf{u}_M = 5|$  in comparison with the case  $|\mathbf{u}_M| = 0$ .

Moreover, with  $|\mathbf{u}_M > 5|$ , the symmetry of the solution changes from dipolar (antisymmetric with respect to the Equator), to quadrupolar (symmetric). For  $\mathbf{u}_M = 10$  a steady non-oscillatory solution takes over.

### Discussion

Solar observations have shown the importance of the non-axisymmetric component of the mean magnetic fields in the formation and evolution of solar activity. Solar dynamo models have so far failed to address the non-axisymmetric features of the solar cycle, most notably the clustering of magnetic activity and preferred longitudes.

We have developed a new kinematic non-axisymmetric mean-field dynamo model of the Sun in spherical geometry, which incorporates the solar rotation as reconstructed from helioseismic data and a model for the meridional circulation. We decompose the magnetic field into its toroidal and poloidal components. This geometry allows waves to propagate azimuthally at different rates for different modes, contrast to a periodic box where only one rate can be allowed. We determine the rotation rate of the first non-axisymmetric mode.

We have considered for simplicity only the lowest azimuthal modes,  $m = 0$  and  $m = 1$ . By the action of a non-axisymmetric  $\alpha$ -effect, the modes are coupled together, and the  $m = 1$  mode shares the same cyclic behaviour as the axisymmetric mode  $m = 0$ .

We have examined three different radial distributions of the mean helicity ( $\alpha$ -effect), two with  $\alpha$  operating near the tachocline and one only near the surface. When the meridional flow is neglected, we found that all produced a cycle with alternating  $m = 0$  and  $m = 1$  modes. The two models with  $\alpha$  near the tachocline both give the ratio  $T/T_{rot}$  of the cycle duration to the rotation rate within 20% of the observed value of 147, whereas the case where  $\alpha$  was concentrated near the sur-



face failed to give agreement indicating that this was not a valid solar model.

The radial profile of  $\alpha$  strongly influences the phase relations between the alternating axisymmetric dipole and the toroidal field intensity at the base of the convection zone.

We determined the rotation rate of the near-surface non-axisymmetric radial field in the three models. The two models with  $\alpha$  close to the tachocline had the same rate of rotation, slightly faster than the core rotation rate, in good agreement with observations. This rate was found to be the same through several cycles. Again, the model with near-surface  $\alpha$  was different, with a rotation rate slower than the core rotation.

The spatial distribution of the non-axisymmetric toroidal fields was found to be concentrated around  $30^\circ$  latitude, where the radial gradient of the differential rotation vanishes. [The latitude, at which the axisymmetric mode is concentrated is higher. However, in axisymmetric dynamos, it is possible to vary the meridional circulation and a latitudinal distribution of  $\alpha$  to lower the latitudinal distribution of toroidal fields (Ruediger & Brandenburg 1995; Dikpati & Gilman 2001). ] When  $\alpha$  was finite near the tachocline, the non-axisymmetric toroidal field had a strong component there. A near surface concentration was also found for all three models.

A preliminary study of meridional circulation indicated that the overall field distribution is not strongly affected, particularly for the toroidal non-axisymmetric component of the field. A bigger effect was found in the cycle period, which becomes longer at higher flow intensities, and the equatorial symmetry of the solutions, which becomes quadrupolar (symmetric) when flow intensity is very high.

In a forthcoming study we will investigate the role of meridional circulation in the non-axisymmetric dynamo in more details .

## Acknowledgements

We are grateful to Axel Brandenburg for his contribution in the developing of the numerical code. We thank Joan Feynman for her careful examination of the manuscript and her advices on the relation between our work and the solar data, and to Marco Velli for helpful discussions. We

thank the reviewer for useful critical comments that resulted in improvement of our paper. This research was conducted in part at the Jet Propulsion Laboratory, California Institute of Technology, under contract with the National Aeronautic and Space Administration. This work was performed while A. Bigazzi held a National Research Council Research Associateship Award at the Jet Propulsion Laboratory.

## A. Description of sources

### A.1. Rotation

The differential rotation is approximated by

$$\Omega(r, \theta) = \frac{\Omega_0}{\Omega_{30}} \left( \Omega_{30}(1 - f(r)) + \Omega_S f(r) \right), \quad f(r) = \frac{1}{2} \left( 1 + \tanh \left( \frac{r - r_\Omega}{\delta_\Omega} \right) \right). \quad (\text{A1})$$

The parameters  $r_\Omega = 0.69$  and  $\delta_\Omega = 0.05$  define the location and the width of the tachocline. Here,  $\Omega_S$  is the surface rotation profile,

$$\Omega_S(\theta) = 1 + a_1 \cos^2 \theta + a_2 \cos^4 \theta, \quad (\text{A2})$$

with  $a_1 = -0.126$ ,  $a_2 = -0.159$ , and  $\theta$  is the co-latitude (Moss 1999; Charbonneau et al. 1999). The equatorial rotation rate is thus given by

$$\Omega_{eq} = \frac{\Omega_0}{\Omega_{30}} \quad (\text{A3})$$

where  $\Omega_{30} = \Omega_S(30^\circ)$ . In all runs we use  $\Omega_0 = 4.9 \times 10^4$ , in non-dimensional units.

### A.2. Diffusivity

The turbulent diffusivity profile is given by

$$\eta(r) = \eta_c(1 - f(r)) + \eta_0 f(r), \quad f(r) = \frac{1}{2} \left( 1 + \tanh \left( \frac{r - r_\eta}{\delta_\eta} \right) \right). \quad (\text{A4})$$

Here,  $r_\eta \equiv r_\Omega = 0.69$ ,  $\delta_\eta = 0.04$ ;  $\eta_c$  and  $\eta_0$  are the diffusivity values in the core and in the convection zone respectively. We use  $\eta_0/\eta_c = 50$  and  $\eta_0/\eta_c = 200$ .

### A.3. $\alpha$ -effect

The radial dependences of the  $\alpha$ -effect for the three cases considered, are:

$$\alpha(r) = \alpha_0 \frac{1}{2} \left( 1 + \tanh \frac{r - r_\alpha}{\delta_\alpha} \right) \quad (\text{A5})$$

with  $\alpha_0 = 0.9$ ,  $r_\alpha = 0.7$ ,  $\delta_\alpha = 0.03$ , in model M1, and  $\alpha_0 = 24.2$ ,  $r_\alpha = 0.9$ ,  $\delta_\alpha = 0.03$  in model M2;

$$\alpha(r) = \alpha_0 \frac{1}{2} \left( 1 + \tanh \frac{r - r_\alpha}{\delta_\alpha} \right) \cdot \frac{1}{2} \left( 1 - \tanh \frac{r - r_\alpha + 0.07}{\delta_\alpha} \right) \quad (\text{A6})$$

with  $\alpha_0 = 1.9$ ,  $r_\alpha = 0.75$ ,  $\delta_\alpha = 0.04$ , for model M3. The values of  $\alpha_0$  have been chosen so that the dynamo is supercritical but close to marginal.

### A.4. Meridional circulation

We consider a simple 2-cell flow where the surface flow amplitude is of the order of that observed. Density stratification in the convection zone is very high, therefore mass continuity has to be taken into account. We specify a simple fit to reproduce the density from a solar model (Christensen-Dalsgaard et al. 1996), between  $0.60R_\odot$  and  $0.95R_\odot$ .

$$\rho = \alpha e^{-\beta r} \quad (\text{A7})$$

where  $\alpha = 247$  and  $\beta = 10.1$ . We impose mass continuity

$$\nabla \rho \mathbf{u} = 0 \quad (\text{A8})$$

by introducing a poloidal potential  $\Psi$  for the mass flow:

$$\rho \mathbf{u} = \nabla \times \nabla \times \hat{\mathbf{r}} \Psi(r, \theta). \quad (\text{A9})$$

The analogous Stokes stream function is  $-r \sin \theta \partial_\theta \Psi$ . Streamlines for this flow are contours where such a function is constant. Fig. 3 shows the two cases of the meridional circulation where the flow does or does not penetrate inside the shear region (tachocline). Those profiles result from a simple power-law expression (Roberts & Stix 1972) for the radial part of the potential:

$$\begin{aligned} \Psi(r) &= \frac{2}{(1-r_b)^6} (r-r_b)^3 (1-r)^3 & r > r_b \\ \Psi(r) &= 0 & r < r_b, \end{aligned} \quad (\text{A10})$$

where  $r_b = 0.45$  for the deep flow case and  $r_b = 0.65$  for the shallower case. We specify the latitudinal dependence to be proportional to

$$P_{2,0}(\cos \theta) \sim 3 \cos^2 \theta - 1 \quad (\text{A11})$$

where  $P_{l,m}$  is the associated Legendre polynomial of order  $l = 2$  and degree  $m = 0$ . This splits the domain into two counter-rotating cells, each poleward of the equator.

## REFERENCES

- Altschuler, M. D., Trotter, D. E., Nekirk, G. Jr., & Howard, R. 1974, *Sol. Phys.*, 39, 3.
- Antonucci, E., Hoeksema, J. T., & Scherrer, P. H. 1990, *ApJ*, 360, 296.
- Bai, T. 1987, *ApJ*, 314, 795.
- Basu S., Antia H. 1997, *MNRAS*, 287,189
- Bigazzi, A. & Ruzmaikin, A. 2003, ESA SP-517: GONG+ 2002. Local and Global Helioseismology: the Present and Future, 12, 239
- Bogart, R. S. 1982, *Sol. Phys.*, 76, 155.
- Benevolenskaya, E. E., Hoeksema, J. T., Kosovichev, A. G., Scherrer, P. 1999, *ApJ*, 517, L163.
- Blackman, E. G. & Field, G. B. 2002, *Phys. Rev. Lett.*, 89, 265007
- Braun, D. C. & Fan, Y. 1998, *ApJ*, 508, L105
- Bullard, E. C. & H. Gellman 1954, *Phil. Trans. Roy. Soc.*, M247, 213.
- Caligari, P. , F. Moreno-Insertis and M. Schüssler 1995, *ApJ*, 441, 886; 1998, *ApJ*, 502, 481.
- Charbonneau, P., & K. B. MacGregor 1997, *ApJ*, 486, 502.
- Charbonneau, P., Christensen-Dalsgaard, J., Henning, R. et al. 1999, *ApJ*, 527, 445.
- Choudhuri, A.R.; Gilman, P. A. 1987, *ApJ* 316, 788
- Choudhuri, A. R. 1989, *Sol. Phys.*, 123, 217
- Choudhuri, A. R., Schussler, M., & Dikpati, M. 1995, *A&A*, 303, L29
- Christensen-Dalsgaard, J. et al. 1996, *Science*, 272, 1286
- de Toma, G., White, O. R., Harvey, K. L. 2000, *ApJ* 529,1101.
- Dikpati, M., & P. Charbonneau 1999, *ApJ*, 518, 598.
- Dikpati, M. & Gilman, P. A. 2001, *ApJ*, 559
- Durney, B. R. 1995, *Sol. Phys.*, 160, 213
- Fan, Y., Fisher, G. H., Deluca, E. E. 1993, *ApJ* 405, 390
- Ferriz-Mas A., Schmitt, D & Shüssler M., 1994, *A&A*, 289, 949
- Ferriz-Mas A., & Shüssler M., 1994, *ApJ*, 433, 852
- Giles, P. M., Duvall, T. L., Scherrer, P. H., & Bogart, R. S. 1997, *Nature*, 390, 52
- Gaizauskas, V. , K. L. Harvey, J. W. Harvey & Zwaan, C. 1983, *ApJ*, 265, 1056.
- Haber, D. A., et al., 2002 *ApJ* 570, 855.
- Harvey, K., & Zwaan, C. 1993, *Sol. Phys.* 148, 85.
- Hathaway, D. H., et al. 1996, *Science*, 272, 1306.
- Hathaway, D. H., D. Nandy, R. M. Wilson, & E. J. Beichmann 2003, *ApJ*, 589, 665.
- Henney, C. J., and J. W. Harvey 2002, *Solar Phys.*, 207, 199.
- Howe, R., J. Christensen-Dalsgaard, F. Hill, R. W. Komm, R. M. Larsen, J. Schou, M. J. Thompson, & J. Toomre, 2000, *Science*, 287, 2456.
- Krause F., Rädler K.-H. 1980, *Mean-field Magnetohydrodynamics and Dynamo Theory*, Akademie Verlag, Berlin.
- Ivanova, T. S., & Ruzmaikin, A. 1985, *Astron. Nachr.*, 306, 177,
- Jones, G. H., Balogh, A., & Smith, E. J. *Geophys. Res. Lett.*, 2003, 30(19).
- Kosovichev, A. G. 1996, *ApJ*, 469, L61.
- Labonte, B. J., Howard, R. 1982 *Solar Physics*, 80 1982, 361.
- Mason, J., D. W. Hughes, & S. M. Tobias 2002, *ApJ*, 580, L89.
- Moffatt, H. K., *Magnetic Field in Electrically Conducting Fluids*, Cambridge Univ. Press, 1978.
- Moss, D., A. Brandenburg & I. Tuominen 1991, *A&A*, 247, 576.
- Moss, D. 1999, *Mon. Not. RAS*, 306, 300.

- Nandy, D., & A. R. Choudhuri 2002, *Science*, 296, 1671.
- Neugebauer, M., Smith, E. J., Feynman, J., Ruzmaikin, A., & Vaughan, A. 2000, *J. Geophys. Res.*, 105, 2315.
- Parker, E. N., 1979 *Cosmical Magnetic Fields* (Oxford: Clarendon Press)
- Roberts, P. H., & Stix, M. 1972, *A&A*, 18, 453.
- Ruediger, G. & Brandenburg, A. 1995, *A&A*, 296, 557
- Ruzmaikin, A. 1998, *Sol. Phys.*, 181, 1.
- Ruzmaikin, A. 2001, *Space Science Reviews*, 95, 43.
- Ruzmaikin, A., Feynman, J., Neugebauer, M., & Smith, E. J. 2001, *J. Geophys. Res.*, 106, 8363.
- Stix, M. 1974, *A&A*, 37, 121.
- Stix, M. 1976, *A&A*, 47, 243
- Tuominen, J. 1941, *Z. Astrophys*, 21,96.
- Vitinskij, J. I. 1969, *Sol. Phys.*, 7, 210
- Wang, Y. M., Sheeley, R. Jr., Nash A. G. 1991, *A&A* 383, 431.

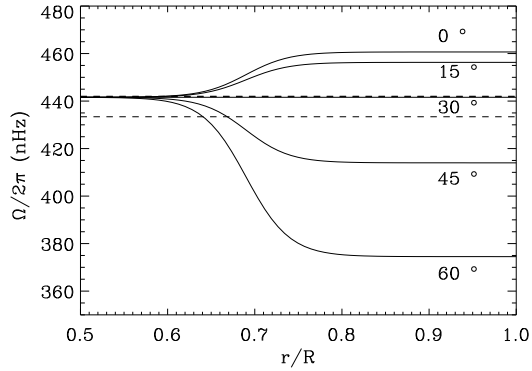


Fig. 1.— Distribution of the internal solar rotation used in our dynamo modeling. Dashed curves show the rotation rates of the non-axisymmetric mode, see Table (1). The upper curve at 442nHz, just above the core rotation rate, is for models M1 and M3. The lower curve, at 433nHz, is for model M2.

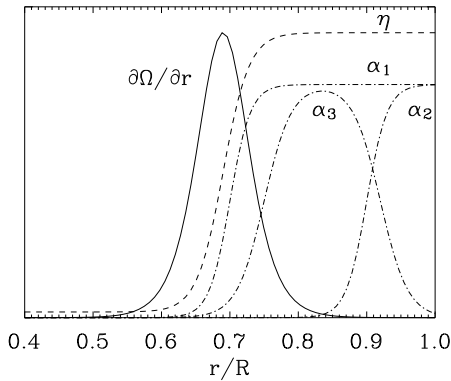


Fig. 2.— Radial distributions of the sources of magnetic field generation:  $\alpha$ , for three different models, the radial gradient of the rotation rate at the equator and turbulent diffusivity  $\eta$ . Values are not to scale; for actual values see Appendix.

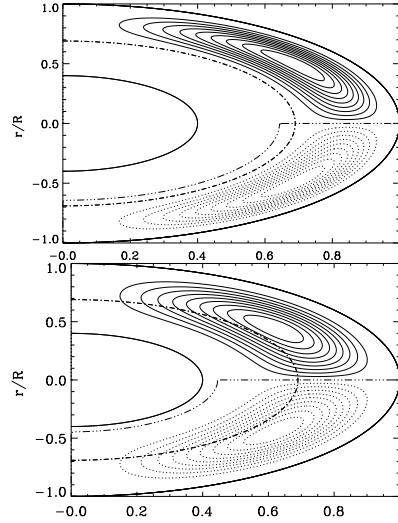


Fig. 3.— Meridional circulation. Flow lines for the two cases considered. Solid lines indicate anti-clockwise flow and dotted lines clockwise. The dashed line at  $0.69R_{\odot}$  indicates the centre of the tachocline.

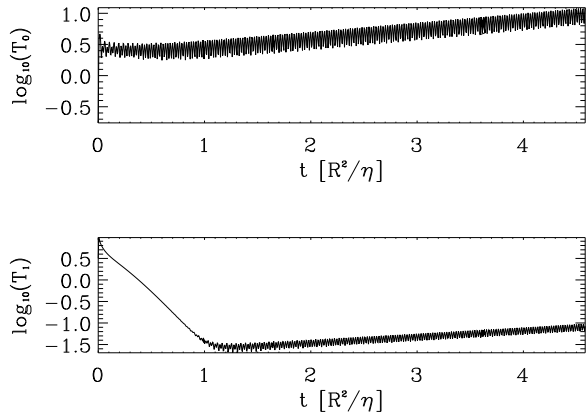


Fig. 4.— Long-term time evolution of the amplitude of the toroidal field potentials for model M1. Top panel is  $T_0$  and lower panel is  $T_0$ . The diffusion time is taken as the time unit.

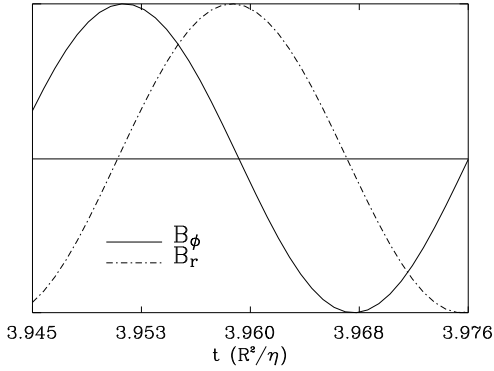


Fig. 5.— Phase relation between magnetic field components in model M3. The time evolution during a cycle of magnetic field components is plotted. The solid line shows the intensity of the azimuthal component of the total magnetic field,  $\mathbf{B}_\varphi^0 + \mathbf{B}_\varphi^1$ , in the meridional plane  $\varphi = 0$ , calculated at the tachocline,  $r = 0.69R_\odot$ , at  $30^\circ$  latitude. The dot-dashed line shows the intensity of the surface radial field component  $\mathbf{B}_r^0$  close to the north pole, at  $80^\circ$  latitude. The phase shift between the fields is  $\pi/2$ . Amplitudes of both toroidal and radial fields are normalised to unity for convenience.

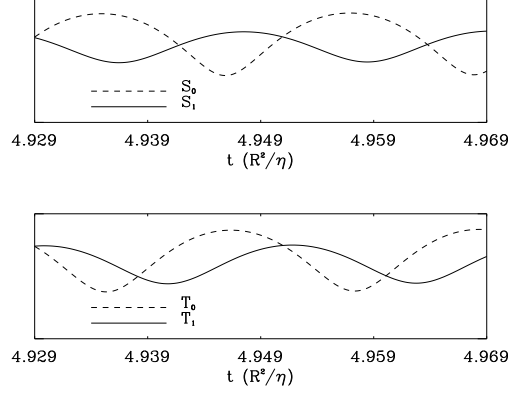


Fig. 6.— Phase relations between poloidal and toroidal components of the axisymmetric and non-axisymmetric magnetic fields for model M1. The integrated square moduli of the scalar potentials  $S, T$ , over the whole domain are plotted versus time. Values are not to scale.  $T_0$  and  $S_0$  are the toroidal and poloidal potentials for the  $m = 0$  mode,  $T_1$  and  $P_1$  are the toroidal and poloidal potentials for the  $m = 1$  mode. The  $S_1$  mode is coupled to the  $T_0$  mode (see Eq. 27). The observed phase relations for the Sun's field components are shown in Fig. 9 for comparison.

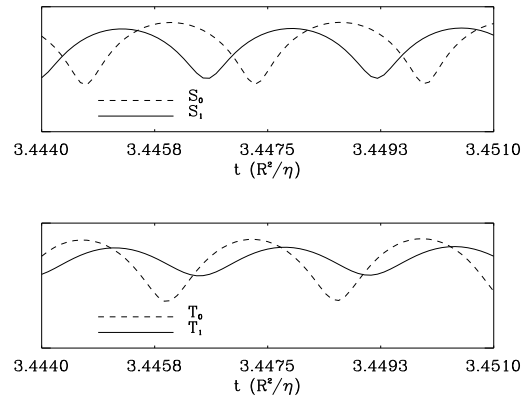


Fig. 7.— Same as in Fig. 6 for model M2.

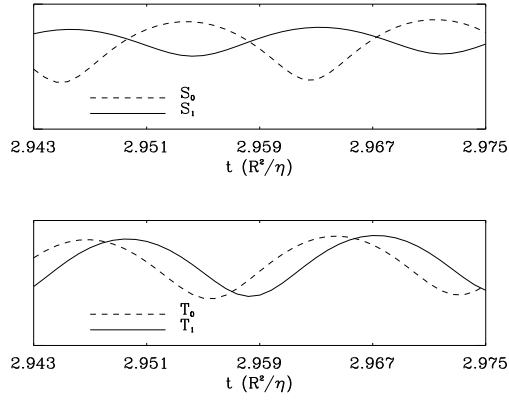


Fig. 8.— Same as in Fig. 6 for model M3.

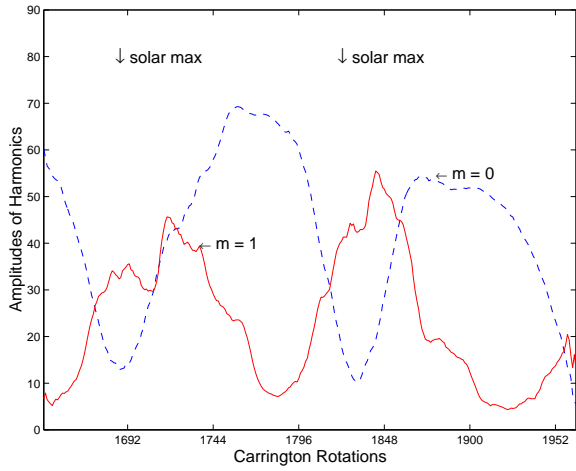


Fig. 9.— Observed phase relations between poloidal components of the axisymmetric (dashed line) and non-axisymmetric (solid line) magnetic field (Ruzmaikin et al. 2001).



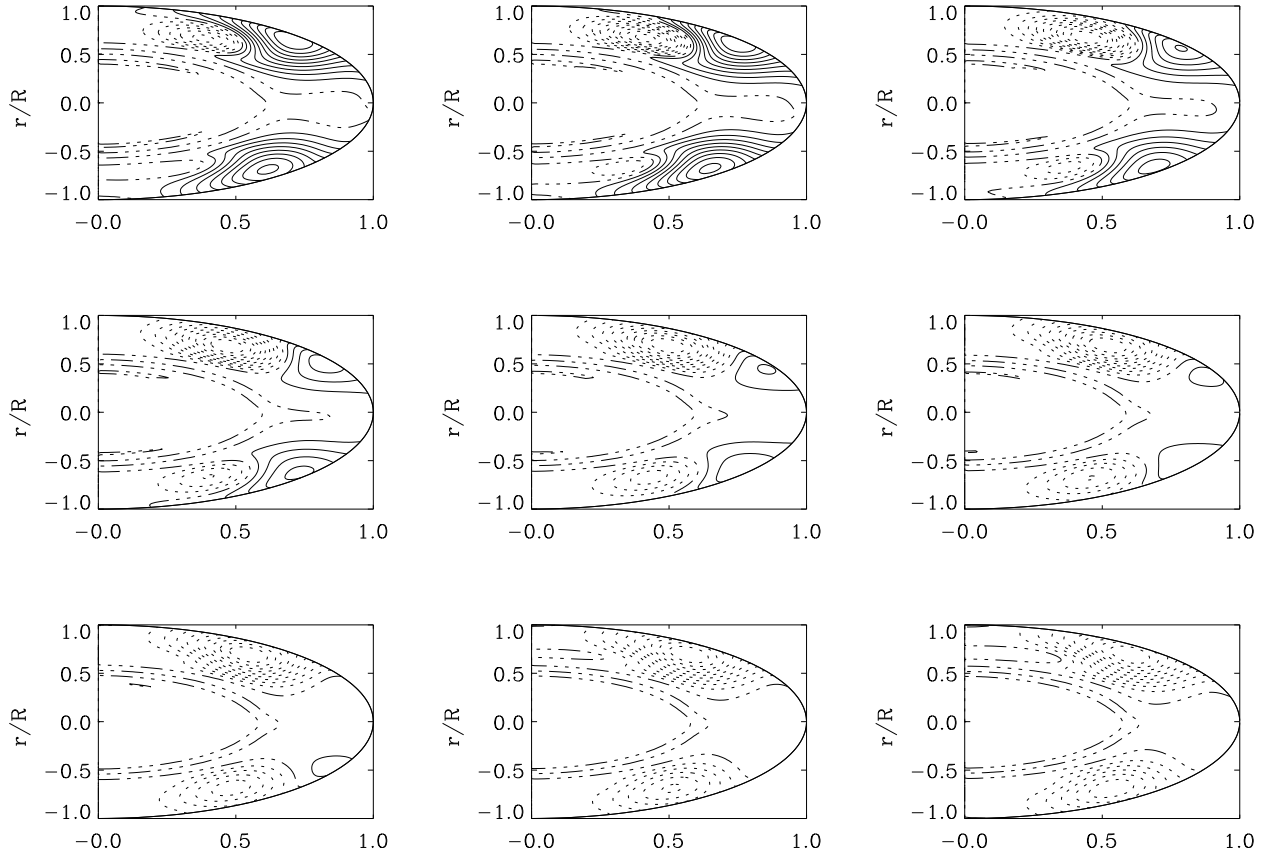


Fig. 10.— Distribution of the axisymmetric ( $m = 0$ ) poloidal field over half a cycle. Time proceeds from left to right and from top to bottom and panels are equally spaced in time. Poloidal field lines are shown. Solid lines have a counter-clock wise direction. Dotted lines mean opposite direction (model M1).

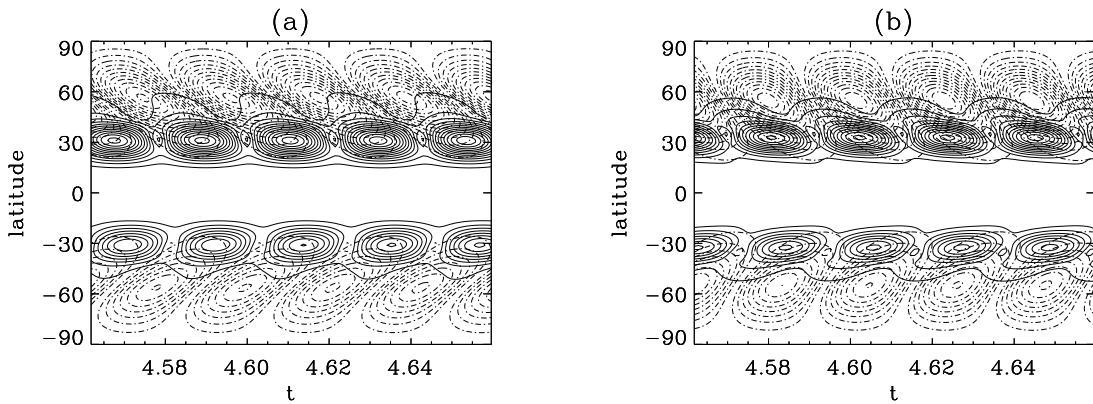


Fig. 11.— Butterfly diagram for the  $m = 0$  (dot-dashed contours) and  $m = 1$  (solid contours) modes of the toroidal magnetic field at two different depths: above the shear layer,  $0.74R_{\odot}$  (a), and in the convection zone, at  $0.85R_{\odot}$  (b). Model M1 is displayed here. The diagram shows the latitudinal distribution of the modulus of the toroidal magnetic field as a function of time, during five half-cycles. The time is measured in unit of the diffusion time.

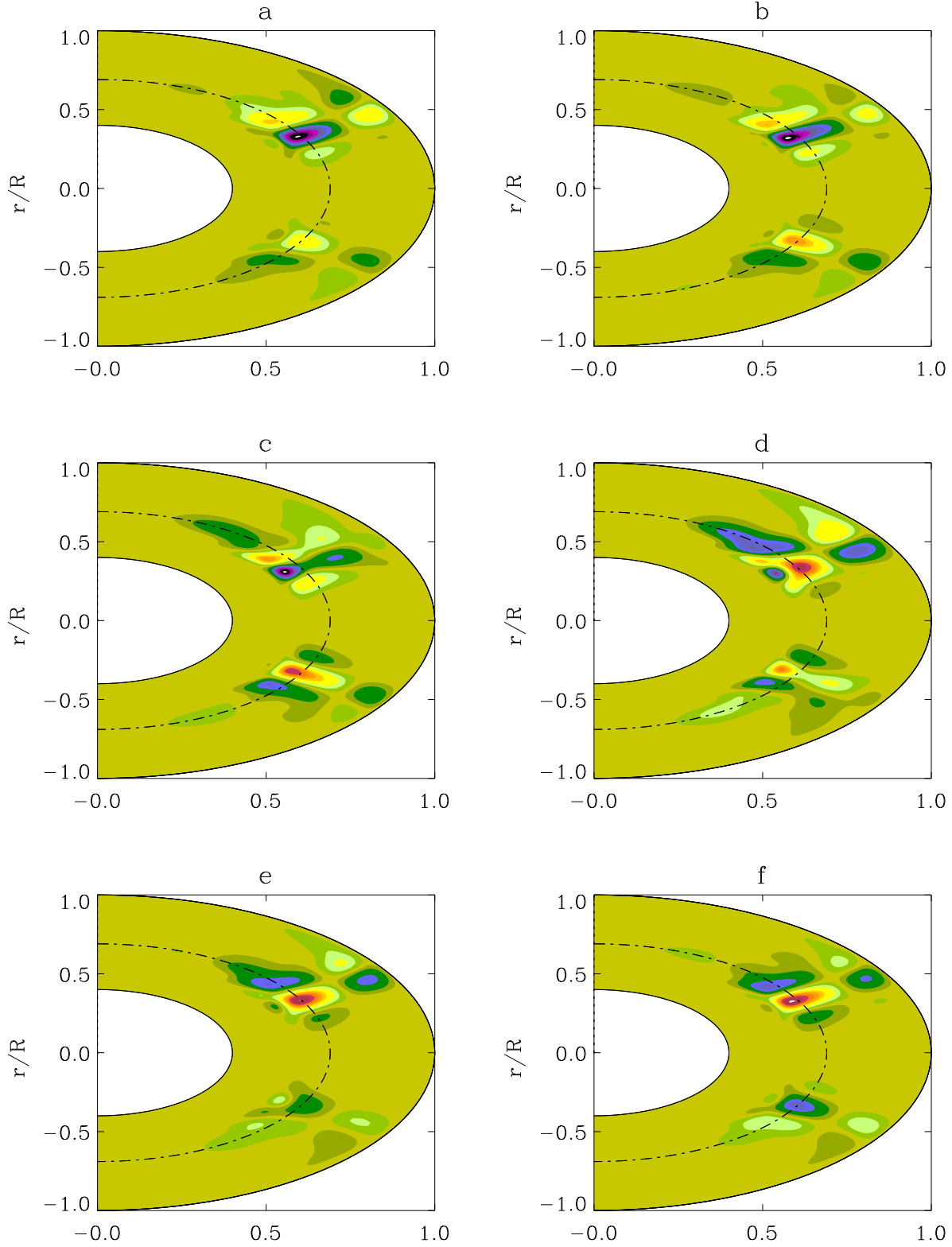


Fig. 12.— Distribution of the non-axisymmetric ( $m = 1$ ) toroidal field through half a cycle, until the field has changed its polarity. Model M1. The contour plot show the intensity of the azimuthal component of the non-axisymmetric field  $\mathbf{B}_\varphi^1$ . The dashed line marks the centre of the tachocline, at  $r = 0.69R_\odot$ , which is also the location of the turbulent resistivity drop.

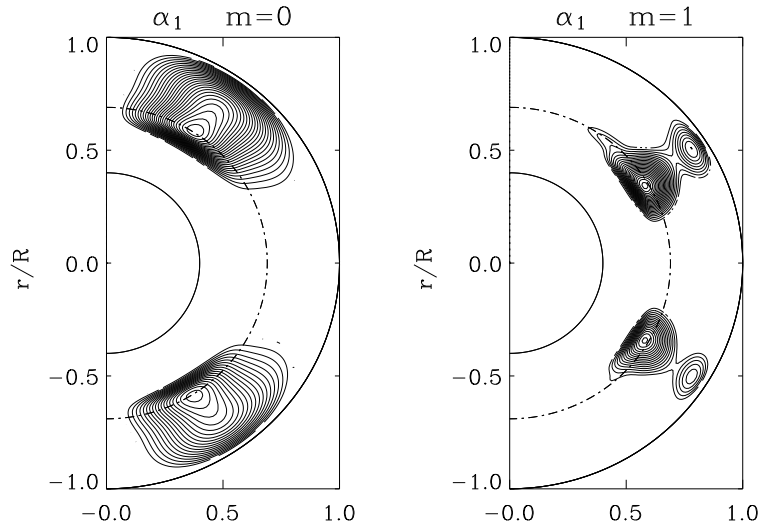


Fig. 13.— Distribution of the axisymmetric ( $m = 0$ ) and non-axisymmetric ( $m = 1$ ) toroidal fields inside the convection zone in model M1. The modulus of the azimuthal component of the magnetic field is shown. Field distribution is integrated over time during a cycle. Contour lines concentrate into region where the field is more intense and resides for longer times. For the  $m = 1$  component, the modulus squared of the field is averaged over the azimuthal direction  $\varphi$ . The dashed line marks the centre of the tachocline, at  $r = 0.69R_{\odot}$  which is also the location of the turbulent resistivity drop.

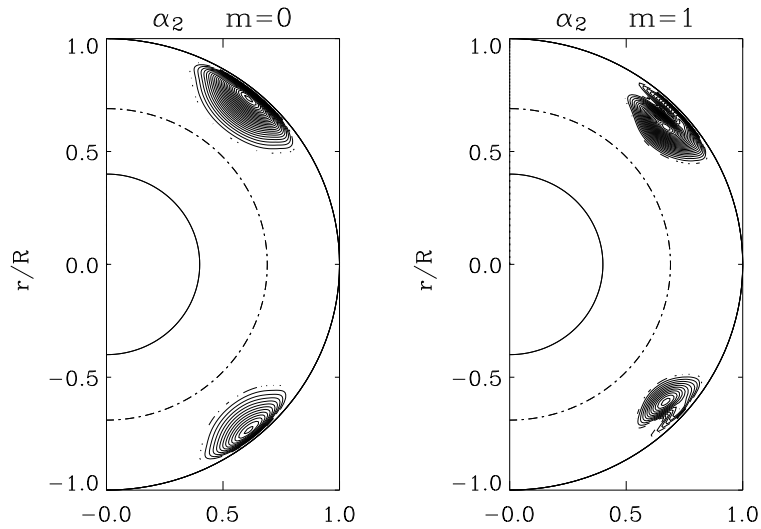


Fig. 14.— Same as in Fig. 13 for model M2.

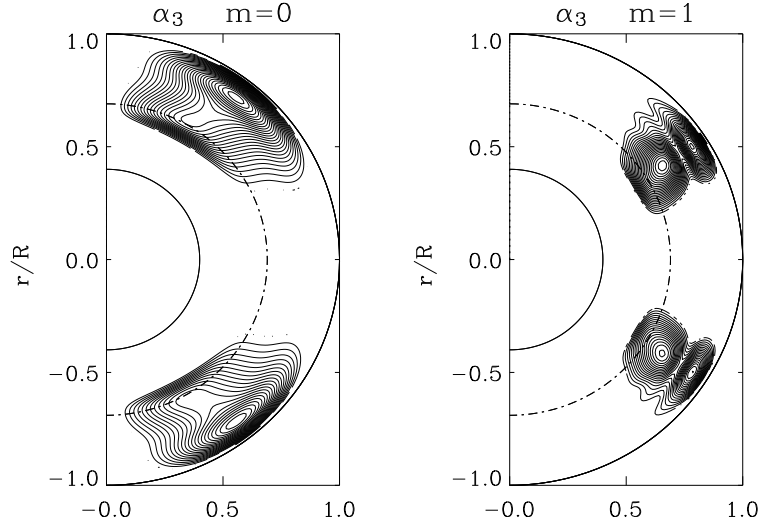


Fig. 15.— Same as in Fig. 13 for model M3.

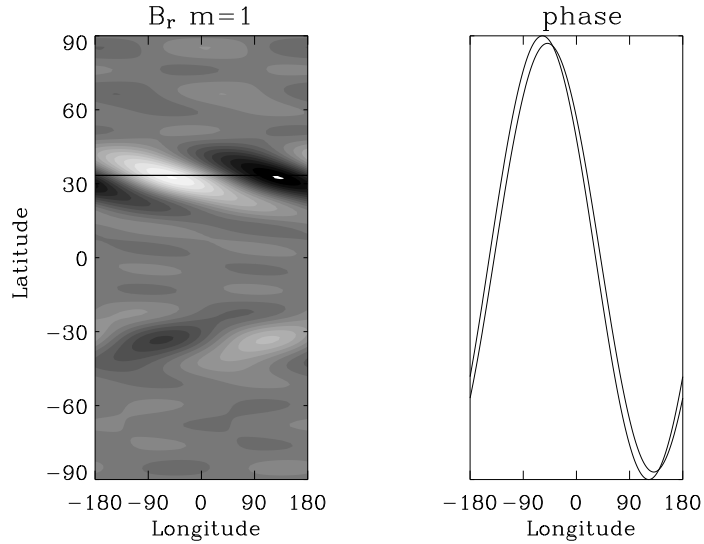


Fig. 16.— Left panel: Near-surface distribution of the radial component of the non-axisymmetric magnetic field at fixed time. White indicates outwardly directed field, black inwardly. Right panel: amplitude of the radial field versus longitude at the latitudinal cut indicated by the line in left panel. Two curves are shown, obtained at different times during a cycle. The phase difference between the maxima divided by the time lag between the two profiles returns the rotation rate of the  $m = 1$  mode.

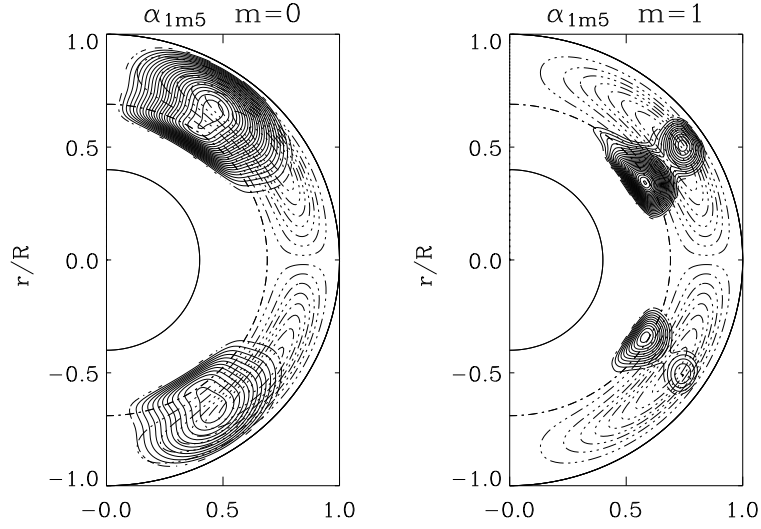


Fig. 17.— Same as in Fig. 13 for model with shallow meridional circulation. The flow lines are superimposed as dot-dashed lines.

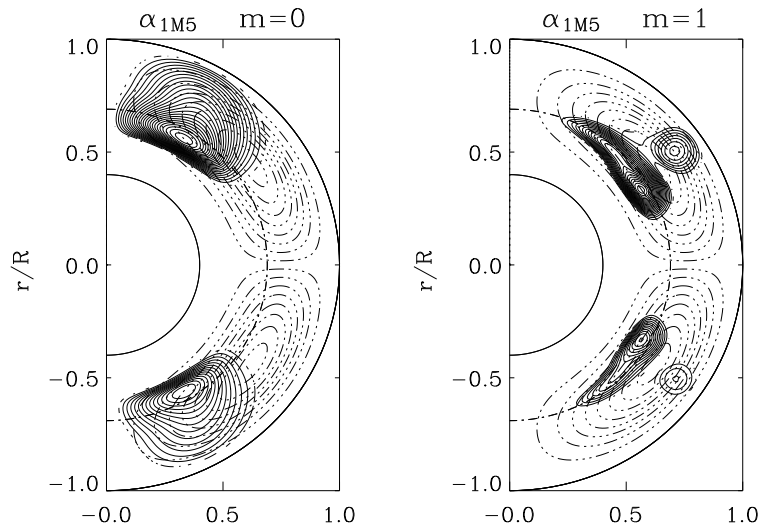


Fig. 18.— Same as in Fig. 13 for model with deep meridional circulation. The flow lines are superimposed as dot-dashed lines.

Model	M1	M2	M3
$\gamma$	0.35	4.15	1.4
$T$	0.022	0.0026	0.018
$T/T_{rot}$	179	20.2	137
$\Omega^1$ (nHz)	442	433	442

Table 1: Time evolution.

Model	M1	M2	M3
$\Delta\varphi (B_\varphi \rightarrow B_r)$	$1/6\pi$	$-3/4\pi$	$1/2\pi$
$\Delta\varphi (S_0 \rightarrow S_1)$	$1.1\pi$	$1.4\pi$	$1.1\pi$

Table 2: Phase relations.

Model	M1	M2	M3
$r_M^0$	0.70	0.95	0.72 ; 0.90
$\theta_M^0(\text{lat})$	57	50	60 ; 52
$r_M^1$	0.67 ; 0.93	0.90 ; 0.97	0.78 ; 0.93
$\theta_M^1(\text{lat})$	30 ; 33	42 ; 41	32 ; 32

Table 3: Location of magnetic field maxima.

Model	M1S	M1D
$r_M^0$	0.80	0.65
$\theta_M^0(\text{lat})$	55	59
$r_M^1$	0.67 ; 0.90	0.65 ; 0.87
$\theta_M^1(\text{lat})$	31 ; 34	30 ; 35

Table 4: Location of magnetic field maxima.